



From Soma to Synapse: Imaging Age-Related Rod Photoreceptor Changes in the Mouse with Visible Light OCT

Pooja Chauhan, PhD,¹ Aaron M. Kho, PhD,² Vivek J. Srinivasan, PhD^{1,2,3}

Purpose: Although the outer nuclear layer (ONL) and outer plexiform layer (OPL) each exhibit a complex internal organization, near-infrared OCT depicts both as monolithic bands. Here, using visible light OCT in the C57BL/6J mouse retina, sublamina age-related changes in photoreceptor features were imaged and interpreted. These features were (1) oscillations in reflectivity, or striations, in the ONL and (2) a moderately reflective subband in the OPL.

Design: Cross-sectional study.

Participants: Pigmented mice (C57BL/6J, n = 14).

Methods: A 1.0- μ m axial resolution visible light spectral/Fourier domain OCT system was used for in vivo retinal imaging. Light and electron microscopy were performed ex vivo. Linear mixed effects models or regression were employed for statistical analysis.

Main Outcome Measures: Comparison of OCT subbands with corresponding histological features, as well as quantification of subband thickness and reflectivity.

Results: Corresponding histological comparisons confirm that striations in the ONL arise from the rowlike arrangement of photoreceptor nuclei and reveal that the moderately reflective OPL subband arises from rod spherules. Compression of outer ONL striations with age suggests changes in soma organization. Thinning of the moderately reflective OPL subband with age supports a reduction of synapses in the OPL. Critically, the ONL somas are tightly correlated with the purported spherule layer but not with the rest of the OPL.

Conclusions: Visible light OCT imaging of the mouse OPL resolves postsynaptic and synaptic differences. Visible light OCT can study rod photoreceptor changes from the soma to the synapse in the living mouse retina.

Financial Disclosure(s): Proprietary or commercial disclosure may be found after the references. *Ophthalmology Science* 2023;3:100321 © 2023 by the American Academy of Ophthalmology. This is an open access article under the CC BY-NC-ND license (<http://creativecommons.org/licenses/by-nc-nd/4.0/>).



Supplemental material available at www.ophtalmologyscience.org.

Loss of vision is a consequence of normal aging. The rod-dominated mouse retina, which is widely used to study degenerative retinal diseases,^{1–3} exhibits myriad quantifiable age-related changes that may contribute to loss of visual function. These include rhodopsin depletion,⁴ outer nuclear layer (ONL) thinning,^{5–8} reduction in ONL rows,^{4,9} reduction in ONL cell count,⁵ diminished electrophysiology,^{4,5,7,9} metabolic changes,⁹ rod spherule retraction,^{10,11} bipolar cell dendritic sprouting,^{10,11} and sex-dependent changes in micro-RNA regulation.⁸ In pigmented C57BL/6J mice, changes such as diminished electroretinograms and ONL row loss are observed as early as 17 months of age⁹ and ONL thinning as early as 12 months of age.⁶ Although photoreceptor loss is usually determined by assessing cell bodies in the ONL, rods and cones also project axons into the outer plexiform layer (OPL), where they form the first synapses of the visual circuit with bipolar and horizontal cells. Age-related OPL thinning, possibly related to

photoreceptor loss, has been documented in the rat^{12,13} and mouse¹¹ but is not commonly reported, likely due to challenges in measuring such a thin layer which is susceptible to tissue processing artifacts.

Near-infrared (NIR) OCT has proven to be useful for phenotyping retinal layer degeneration in living mouse models,^{14,15} typically by measuring ONL or retinal thickness. In NIR OCT, the photoreceptor somas in the ONL and their connections in the OPL each appear as monolithic bands. Yet, histologically, the ONL and OPL are far from monolithic. The ONL is organized into rows of photoreceptor cell somas,^{4,9} characterized by heterochromatin clumps (HCs).¹⁶ The OPL is divided into distinct compartments,¹¹ with an outer, synaptic compartment containing rod spherules and an inner, postsynaptic compartment containing horizontal and bipolar cell dendrites and processes.^{17,18}

Two decades ago, visible light OCT was demonstrated to improve axial resolution.¹⁹ Although a number of in vivo

ophthalmic applications of visible light OCT emerged over the past decade,^{20–25} identifying new retinal subbands or features has been challenging. A careful consideration of the unique technical challenges posed by visible light OCT^{26–28} has recently enabled true 1.0- μm resolution retinal imaging. These efforts have led to the revelation of new photoreceptor features in mice²⁹ and humans.³⁰ First, as shown previously,²⁹ visible light OCT reveals reflectivity oscillations, appearing as horizontal image striations within the outer ONL, arising from the rowlike arrangement of photoreceptor nuclei in mice. Second, we report here that visible light OCT also depicts a moderately reflective OPL subband (meso-OPL) just inner to the hyporeflective ONL and outer to the more highly reflective portion of the OPL (hyper-OPL). We show here that the meso-OPL aligns on histology with rod spherules, which are sites of synapses between rods, horizontal cells, and bipolar cells¹⁶ in the OPL.

Next, we investigate changes in these new visible light OCT features and their associations with well-established age-related ONL thinning in a cohort of C57BL/6J mice, a common inbred strain used as a background for genetic models of human disease. The aging retina was chosen as a model in this work because rod photoreceptor loss is subtle,⁹ presenting a challenge for our noninvasive imaging approach. At the same time, age-related rod photoreceptor loss is clinically relevant,^{31–33} and the rod-dominated mouse retina is a reasonable model of the human retina at 15° to 20° eccentricity in terms of rod-to-cone ratios,³⁴ albeit with some differences in age-related photoreceptor loss.⁶ Novel methods for assessing photoreceptor synapses and soma organization may complement standard OCT ONL thickness measures, helping to provide a more complete picture of retinal aging.

Materials and Methods

Imaging

A free-space visible light spectral/Fourier domain OCT system was used for *in vivo* retinal imaging of C57BL/6J ($n = 14$, 9.34 ± 7.01 months, 10 males, 4 females) mice from The Jackson Laboratory. The light microscopy (LM) was performed on 3 of the C57BL/6J mice (2.5 months old, 4.5 months old, and 19 months old). The study was endorsed by the UC Davis Institutional Animal Care and Use Committee, and performed in accordance with the Association for Research in Vision and Ophthalmology, National Institute of Health, and Animal Research: Reporting of *In Vivo* Experiments guidelines.

As previously described,²⁹ mice were initially anesthetized with 2% to 5% isoflurane in a gas mixture of 80% air and 20% oxygen. Tropicamide was applied topically for cycloplegia, and then, saline drops were applied for imaging. Imaging was performed under 1% to 2% isoflurane anesthesia at 10 to 30 kHz axial scan rate. Prior to acquisition, the eye was aligned for 1 to 2 minutes by illuminating only with the red portion of the visible light spectrum to minimize bleaching. After verifying the corneal reflex the mouse was translated axially to generate a retinal image. The full spectral width, axial resolution, and lateral resolution in tissue were 259 nm, 1.0 μm , and 7.6 μm , respectively. For speckle reduction, 8 repeated volumetric datasets were acquired with 512 a-lines and 64 b-scans with a 1.20-mm or 1.44-mm fast axis range and a

0.12-mm slow axis range. OCT volumes were oriented with a fast temporal-nasal axis and a slow inferior-superior axis and located approximately 1 mm superior to the optic nerve head. Each volumetric dataset was acquired in 26.2 seconds with 300 μW of incident power.

Data Processing

The raw OCT interference fringes were mean-subtracted and then resampled to linear vacuum wavenumber space, followed by approximate spatially-independent dispersion compensation, Fourier transformation, coarse axial and lateral motion correction, spatially dependent dispersion compensation,²⁶ finer axial motion correction, and spectral shaping. Image quantification procedures were tailored to preserve the fine axial resolution present in the raw images to the extent possible. The OCT images were averaged along the slow (y) axis (Fig 1A) and corrected for the noise offset. As shown in Figure 1A, B, the OPL was revealed to consist of a hyper-OPL and a meso-OPL. The inner and outer borders of the hyper-OPL were manually drawn (Fig 1C). The meso-reflective outer OPL (meso-OPL) exhibited an approximately linear reflectivity decrease from the hyper-reflective inner OPL to the ONL (Fig 1B, D). At each transverse location, the outer border of the meso-OPL was detected as the position of the slope discontinuity of the best continuous bilinear fit to the axial reflectivity profile (Fig 1D).

Striations in the outer ONL (Fig 1E) appeared as reflectivity peaks and valleys (Fig 1F) that could be detected and quantified by careful alignment and averaging. Using line profiles from 2-times upsampled datasets, at each transverse location, the region near the external limiting membrane (ELM) (Fig 1E, F) was fitted with a Gaussian, representing the ELM reflectivity, plus an offset, representing the ONL reflectivity. Those locations with $R^2 > 0.90$ and Gaussian standard deviation < 4 pixels were retained (e.g., Fig 1G). After normalization to the offset, all retained axial profiles were averaged, yielding a relative intensity profile (e.g., Fig 1H). This relative ONL intensity profile was fitted with a polynomial of order 7 for ascertaining both the first valley and the first peak of ONL reflectivity (Fig 1H). Linear mixed effects models, accounting for correlation between eyes, as well as between imaging locations, or simple regression were employed for statistical analysis.

Histological Processing

As previously described,²⁹ the superior pole of the eye was first marked, and the eye was then enucleated and fixed overnight. The lens was removed, and the eye was separated into posterior and anterior parts with dissection of the posterior eye cup, while maintaining orientation. The optic disk was used as a landmark to sample near the imaged location. The tissues were rinsed by sodium phosphate buffer and osmium tetroxide and dehydrated as previously described.²⁹ Reinfiltration of the tissues was accomplished in half resin/half propylene oxide overnight, prior to infiltration in 100% resin the next day. For LM, after polymerization, the embedded tissues were sectioned with an ultramicrotome (Leica EM UC6) and stained with 1% toluidine blue. For electron microscopy (EM), the tissues were also sectioned with an ultramicrotome and stained with 4% uranyl acetate and 0.3% lead citrate in 0.1 N sodium hydroxide. An upright Nikon microscope with a 100-times-magnification objective was used to take LM photographs. Electron microscopic images of the sample were captured at 1250-times or 2600-times magnification by a Talos L120C transmission electron microscope. All other LM and EM details have been described previously.²⁹

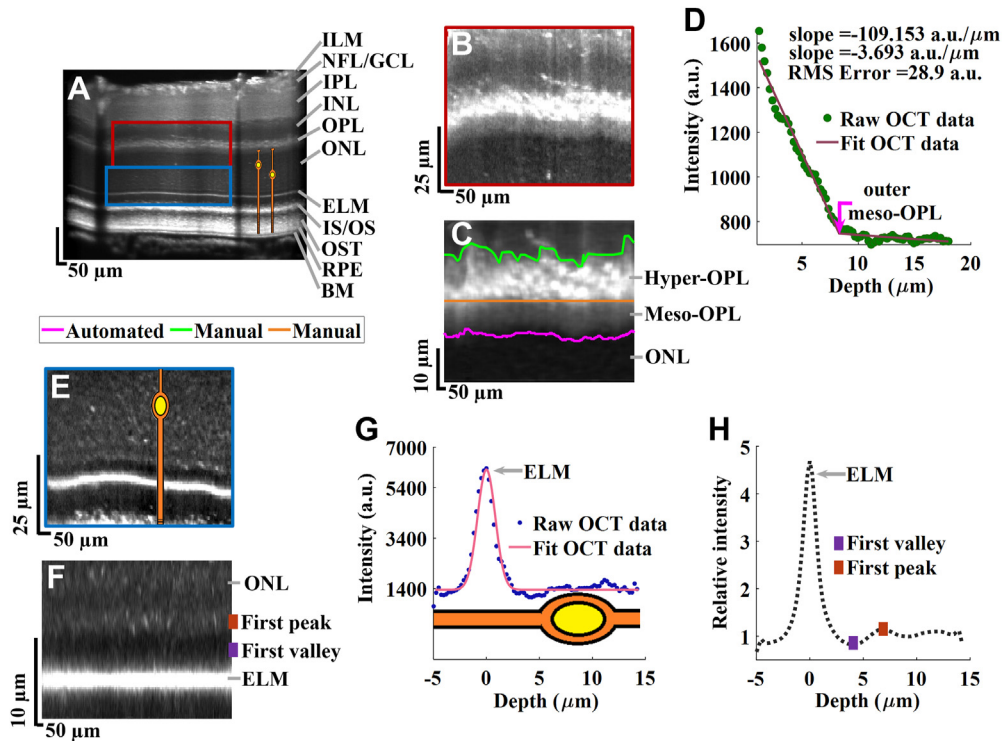


Figure 1. Segmentation of meso-outer plexiform layer (OPL) and analysis of outer outer nuclear layer (ONL) striations. **A**, Visible light OCT image of a 3-month-old mouse retina. OPL zoom (**B**) and further flattened OPL zoom (**C**) with segmentation of hyperreflective (hyper-OPL) and meso-reflective (meso-OPL) subbands. **D**, Automated outer meso-OPL boundary detection. Each transverse position is normalized to the median ONL signal in the **C** panel. ONL zoom (**E**) and further outer ONL zoom image of selected axial profiles (see [Materials and Methods](#) for selection criteria) (**F**) with external limiting membrane (ELM) flattening to visualize the subcellular reflectivity features (first valley and first peak) within the ONL. **G**, OCT intensity profile with fit (Gaussian plus offset, $R^2 = 0.97$). **H**, Averaged relative ONL intensity profile across image according to the criteria described in the text. Each transverse position is normalized to the offset in the **F** and **H** panels. Depth is positive into the ONL. Zoomed OCT images in panels **B** and **E** are deshadowed by normalizing to the median ONL intensity at each transverse position. BM = Bruch's membrane; GCL = ganglion cell layer; ILM = internal limiting membrane; INL = inner nuclear layer; IPL = inner plexiform layer; IS/OS = inner segment and outer segment junction; NFL = nerve fiber layer; OST = photoreceptor outer segment tips; RPE = retinal pigment epithelium.

Photoreceptor somas in the ONL are visualized in LM as HCs. Rod somas possess 1 large HC, whereas cone somas (located mainly in the outer ONL) exhibit multiple irregularly shaped HCs.¹⁶ Photoreceptor axons from the ONL form synapses with bipolar and horizontal cells in the OPL. The depths (perpendicular distances) of HCs relative to the outer OPL were quantified from LM. The outer OPL boundary was delineated manually and fitted with a third-order polynomial. The positions of nuclear HCs in the ONL were manually marked, and distances were measured perpendicular to the outer OPL boundary. The counts were binned in 1- μ m depth increments, and density was calculated by dividing the count number in a bin by the bin width and the outer OPL length in micrometers.

Results

Histological Comparison and Image Interpretation

To establish a foundation for image interpretation, visible light OCT (**Fig 2A, B**) was compared with LM and EM (**Fig 2C, D**), with scale bars determined independently for each modality. A preliminary qualitative comparison suggested that the hyper-OPL corresponded to the plexus of

postsynaptic bipolar and horizontal cell dendrites and processes,¹⁷ and dense OPL microvasculature. The meso-OPL corresponded with rod spherules, the sites of ribbon synapses.

To strengthen these preliminary associations, we sought to find a correspondence between the dip in reflectivity outer to the meso-OPL and the first row of cell nuclei outer to the rod spherules. Such a correspondence would be expected since Chauhan et al²⁹ showed that rows of nuclei coincide with hyporeflective striations in the outer ONL (see also **Fig S3**). A total of 1400 ONL HCs were marked in 6 LM images near the imaged OCT location. The distance from each HC to the manually drawn outer OPL boundary was determined on LM (**Fig 2E**). After convolving the depth distribution (**Fig 2E**) with the estimated OCT point spread function, the peak in nuclear HC density was found to align well with the dip in OCT intensity at the inner edge of the ONL (**Fig 2G**). Because the innermost row of ONL nuclei lies just outer to the rod spherules and the dip in reflectivity lies just outer to the meso-OPL OCT subband, our hypothesis that the meso-OPL arises from rod spherules is strengthened. More generally, the inner ONL dip adds to the body of evidence (**Fig S3**)²⁹ that the rowlike

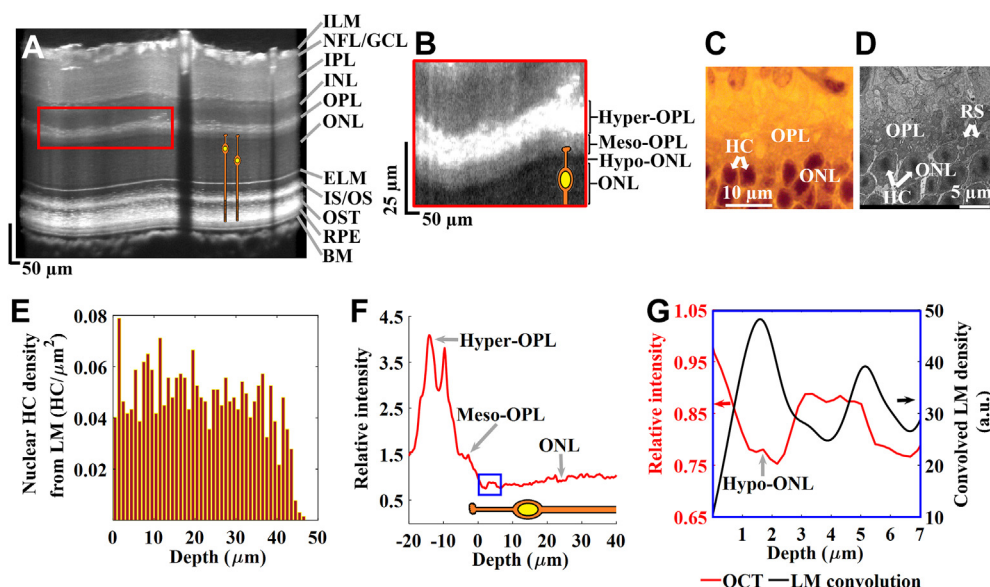


Figure 2. Correlative evidence for rod spherules in visible light OCT. **A**, Visible light OCT image of a 2.5-month-old mouse retina with **(B)** zoomed image of hyperreflective (hyper-outer plexiform layer [OPL]), meso-reflective (meso-OPL), and outer nuclear layer (ONL) bands. Zoomed **(C)** toluidine blue light microscopy (LM) and **(D)** electron microscopy (EM) sections from the same retina. **E**, Nuclear heterochromatin clumps (HC) depth distribution, with positive depth outer to the OPL. **F**, Averaged relative OPL and ONL intensity. **G**, Zoomed averaged relative meso-OPL intensity with convolved LM density. Depth is positive into the ONL. Zoomed OCT image in panel B is deshadowed by normalizing to the median ONL intensity at each transverse position. BM = Bruch's membrane; ELM = external limiting membrane; GCL = ganglion cell layer; ILM = internal limiting membrane; INL = inner nuclear layer; IPL = inner plexiform layer; IS/OS = inner segment and outer segment junction; NFL = nerve fiber layer; OST = photoreceptor outer segment tips; RPE = retinal pigment epithelium; RS = rod spherules.

arrangement of ONL somas leads to striations in OCT intensity. Naturally, the striations are most prominent where the rows are most pronounced, specifically, at the outer²⁹ and inner (Fig 2G) ONL boundaries.

Cross-sectional Aging Study

First, a qualitative image comparison (Fig 4) showed that the meso-OPL appears markedly attenuated in the older mouse (Fig 4D, G), whereas the outer ONL striations appear slightly compressed with hyperreflective dots (Fig 4E, H).

Next, changes in the new visible light OCT features with age were systematically investigated and benchmarked against ONL thinning, which has been well documented. Outer nuclear layer thickness measured by visible light OCT decreases with age (Fig 5A, B), as expected. Both the first ONL reflectivity valley and peak move closer to the ELM with age (Fig 5C, D), whereas the relative intensity of the first ONL peak but not the first ONL valley increases with age (Fig 5E, F). Both the first ONL valley and first ONL peak are tightly correlated with the ONL (Fig 5G, H) and with each other (Fig 5I). The meso-OPL subband thickness decreases with age (Fig 6A, B), with no change in the hyper-OPL subband thickness with age (Fig 6C). The ONL correlates with the meso-OPL (Fig 6D) but not the hyper-OPL (Fig 6E) across mice. The meso-OPL correlates negatively with the hyper-OPL (Fig 6F).

One potential confound is that age-related changes in image quality may impact quantitative measurements. Therefore, meso-OPL findings were verified in 2 ways. First, the outer boundary of the meso-OPL was manually

drawn and compared with the automatically detected outer meso-OPL boundary. Importantly, the manually drawn meso-OPL thickness was also found to decrease with age (Fig S7A). Furthermore, the meso-OPL measurements from manual and automated outer boundaries agreed, with $0.99 \pm 1.64 \mu\text{m}$ limits of agreement (Fig S7B). Second, the image quality of meso-OPL band was benchmarked by the contrast-to-noise ratio (CNR), defined as the OCT difference between the median meso-OPL and median ONL intensities, divided by sum of their respective variances along the transverse direction. The meso-OPL CNR measured by visible light OCT decreases with age (Fig S7C), but critically, CNR could not explain the meso-OPL thickness measurement (Fig S7D). The verification of our meso-OPL thickness measurements and the lack of correlation between meso-OPL thickness and CNR bolster that confidence meso-OPL thinning with age is an anatomical change, not an imaging or segmentation artifact.

Discussion

Advances in Retinal Imaging Science

First, this study adds to the body of evidence that visible light OCT can image density variations of HCs in the ONL in mice. This ability is now supported in the outer ONL by EM²⁹ and by LM (Fig S3), as well as in the inner ONL by LM (Fig 2G). A simple explanation for the observed inverse relationship between reflectivity and density is one of mutual exclusion. Specifically, due to their large size,³⁵

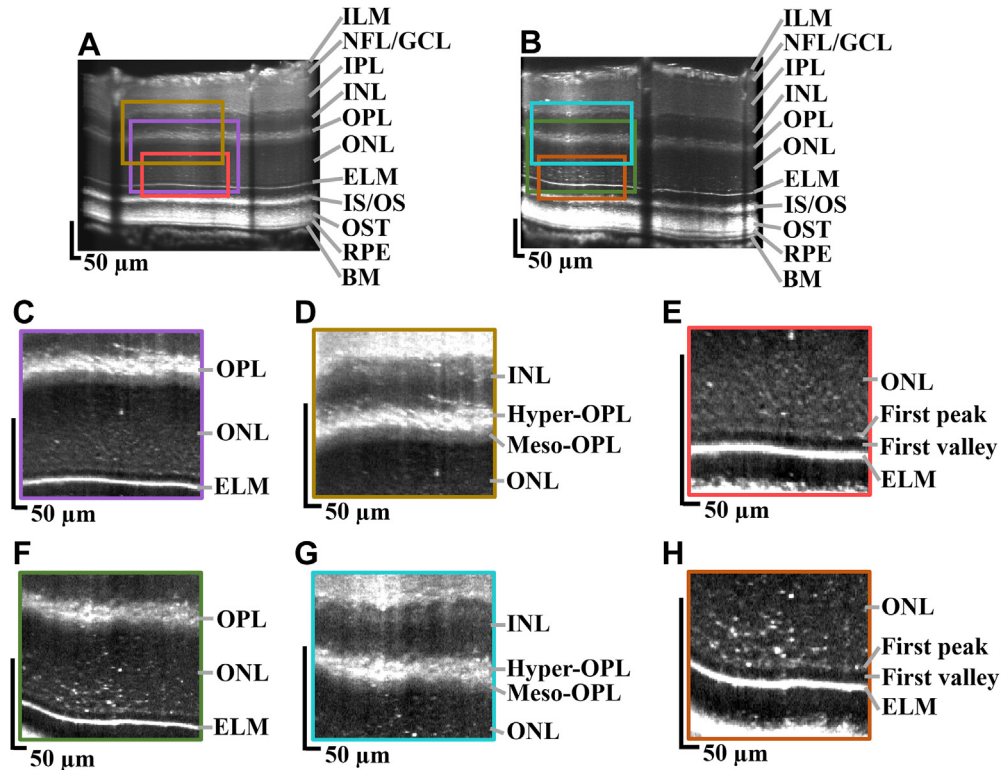


Figure 4. Comparison of meso-outer plexiform layer (OPL) subband and outer outer nuclear layer (ONL) striations in mice of different ages. Visible light OCT image of (A) 3-month-old and (B) 19-month-old mouse retinas. Zoomed image of OPL, ONL, and external limiting membrane (ELM) in (C) 3-month-old and (F) 19-month-old retinas. Zoomed image of inner nuclear layer (INL), hyperreflective (hyper-OPL), and meso-reflective (meso-OPL) bands in (D) 3-month-old and (G) 19-month-old retinas. Zoomed image of ELM and outer ONL to visualize the first valley and first peak of ONL reflectivity in (E) 3-month-old and (H) 19-month-old retinas. Zoomed OCT images in C–H panels are deshadowed by normalizing to the median ONL intensity at each transverse position. BM = Bruch’s membrane; GCL = ganglion cell layer; ILM = internal limiting membrane; IPL = inner plexiform layer; IS/OS = inner segment and outer segment junction; NFL = nerve fiber layer; OST = photoreceptor outer segment tips; RPE = retinal pigment epithelium.

HCs are assumed to be less backscattering per unit volume than other non-HC ONL constituents, which include nuclear membrane, lamina, euchromatin,^{36,37} photoreceptor axons, and Müller cell processes. Thus, any depth with relatively more HCs will presumably have a relatively lower volume fraction of said non-HC constituents and, therefore, lower reflectivity than any depth with relatively fewer HCs.

Second and perhaps most importantly, this study demonstrates that visible light OCT distinguishes synaptic and postsynaptic subbands within the OPL. Our subband assignment is informed by anatomical evidence from LM and EM that the meso-OPL aligns with rod spherules (Fig 2). The result that the meso-OPL is tightly coupled with the ONL (Fig 6D) strengthens the notion that both arise from the rod photoreceptor cell. On the other hand, the uncoupling between the hyper-OPL subband and the ONL (Fig 6E) is consistent with them being 1 synapse apart and potential reflectivity contributions from dense microvasculature.³⁸ There are several interpretations of the negative correlation between the hyper-OPL and meso-OPL (Fig 6F). One possibility is a volume compensation for loss in synapses by an expansion of the postsynaptic plexus. Another possibility is error in manually drawing the shared boundary, which would increase one subband

while decreasing the other. Nonetheless, this divergence between subbands underscores the importance of assessing each individually, as proposed here. Finally, the underlying reasons for OPL stratification on visible light OCT are not fully clear. Second harmonic generation studies³⁹ imply that the meso-OPL space is devoid of axons with polarized microtubules. Mitochondria should be investigated as sources of reflectivity in the OPL,⁴⁰ in addition to other factors such as microvasculature and neurite size, density, and orientation.

Age-related Rod Photoreceptor Changes

Notably, the imaging results provide a window into age-associated photoreceptor changes in mice. Some of the feature shifts are subtle, as small as 1/40th of a micrometer per month (Fig 5C), and yet can be detected by our methodology. As discussed above, the meso-OPL subband, purported here to arise from rod spherules, was markedly attenuated in older mice. Thinning with age was readily quantifiable. Although both rod and cone pathways may be affected in early aging in the mouse,⁶ we assume that OCT bands in the mouse are more indicative of rods, which comprise 97% of photoreceptors.¹⁶ In particular,

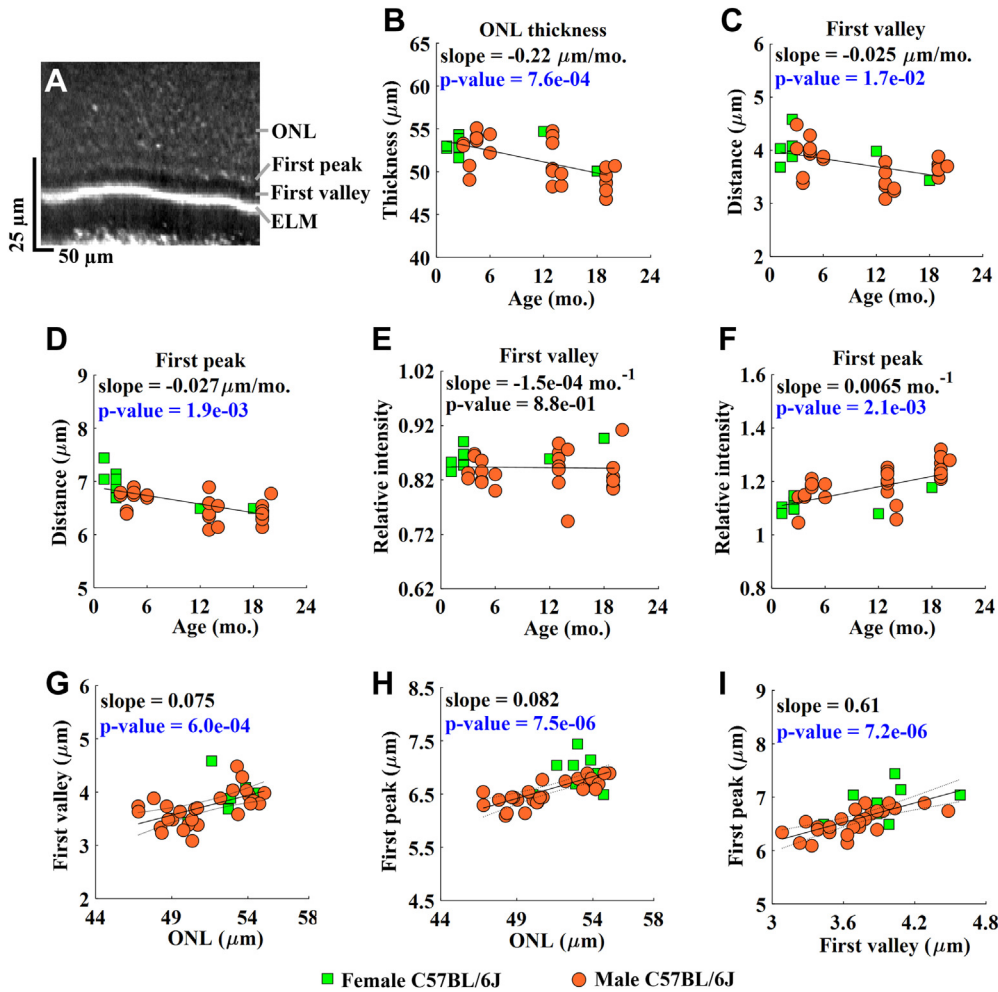


Figure 5. A, Zoomed visible light OCT image of a 3-month-old mouse retina with outer nuclear layer (ONL) striations (first valley and first peak) and external limiting membrane (ELM). Linear mixed effects models for (B) ONL thickness, (C) first valley, (D) first peak distance versus age, as well as (E) first ONL valley and (F) first ONL peak relative intensities versus age. Linear regression for (G) first valley, and (H) first peak distance versus ONL thickness, as well as (I) first ONL peak distance versus first ONL valley distance. Zoomed OCT image in panel A is desaturated by normalizing to the median ONL intensity at each transverse position.

rod OPL spherule synapses form a thick layer outer to a thin row of cone terminals in the mouse.¹⁸ Therefore, meso-OPL thinning is likely to arise from a rarefaction of rod spherules in the OPL. This reduction may be attributed in part to synapse loss. Synapse loss accompanies photoreceptor loss with age, although synapse loss itself is rarely measured directly.⁴¹ Additionally, spherule retraction is well documented in aged mice^{10,11,17,41} and may contribute to meso-OPL thinning. This suggests that measuring the ONL and meso-OPL independently could provide more information than measuring just the ONL. Along these lines, a possible rarefaction is observed in the rod spherule layer histologically (Fig S8). These changes may be susceptible to histological processing artifacts. Interestingly, the reflectivity ratio of the meso-OPL to the inner ONL and the reflectivity ratio of the hyper-OPL to the meso-OPL also decreased with age (Fig S9). These trends suggest that the OPL is attenuated relative to the ONL with age. Whether synaptic changes can be detected earlier than

photoreceptor soma loss by visible light OCT, remains unknown.

The changes in the intensity striations of the outer ONL with age are more difficult to interpret. As discussed above, HC density variations underlie the striations, with lower density explaining higher intensity and vice versa. Therefore, constriction of outer ONL striations with age (Fig S10) supports a tighter arrangement of cell nuclei. Whether this “rearranging” accompanies changes in cell nuclear size or morphology³⁷ is unknown. Overall, results show that outer ONL remodeling occurs in concert with age-related cell loss, implying that thinning of the ONL may result not only from a loss of cell rows but also from a more compressed arrangement of rows in the outer ONL. If the arrangement of nuclei changes, standard metrics of ONL row number and thickness may not always agree.

The above discussion suggests that ONL reflectivity should report on HC density. Practically, relative ONL

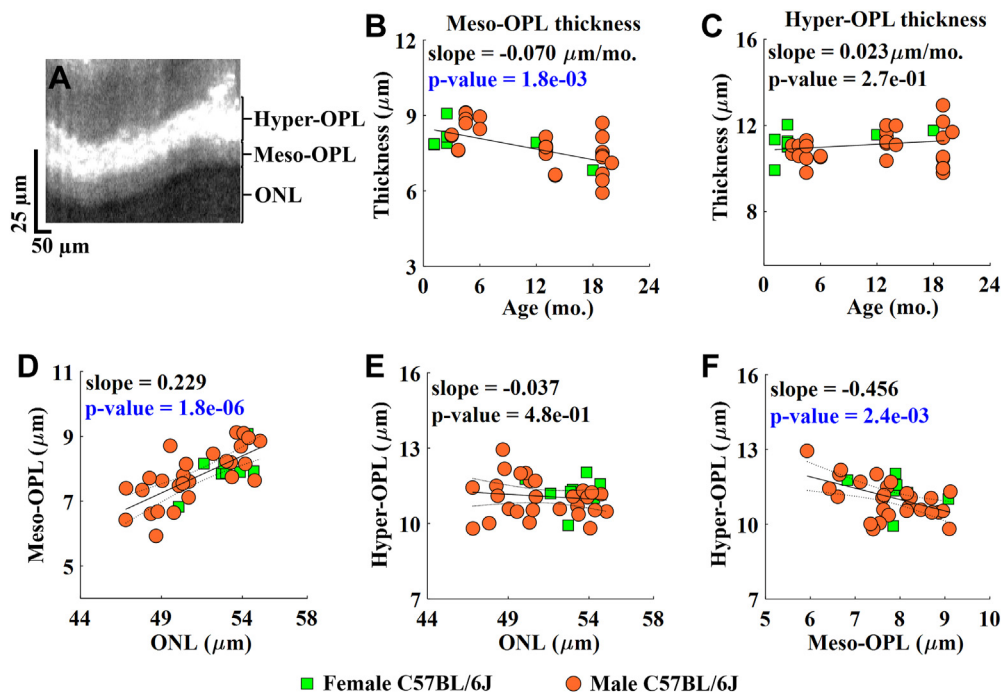


Figure 6. A, Zoomed visible light OCT image of a 2.5-month-old mouse retina with hyperreflective (hyper-outer plexiform layer [OPL]), meso-reflective (meso-OPL), and outer nuclear layer (ONL) bands. Linear mixed effects models for age-related changes in the (B) meso-OPL and (C) hyper-OPL. Linear regression for (D) meso-OPL versus ONL thickness, (E) hyper-OPL versus ONL thickness, and (F) hyper-OPL versus meso-OPL thickness. Zoomed OCT image in panel A is deshadowed by normalizing to the median ONL intensity at each transverse position.

intensity after normalization was analyzed, which relates to relative HC density. The relative intensity of the first peak was found to increase with age (Fig 5F). One explanation could be changes in HC density between rows in older mice. Another explanation could be related to the appearance of hyperreflective dots in the outer ONL in older mice (e.g., Fig 4F), whose origins remain unclear. Similar ONL hyperreflective dots have been attributed to microglia in mouse⁴² and human studies.^{43,44} Although questions remain, the data clearly support that visible light

OCT affords new ways of measuring rod photoreceptor loss and remodeling at the soma and synapse. Such information may be challenging to glean from histology, which is subject to processing artifacts⁴⁵ that distort the arrangement of nuclei (e.g., Fig S3).

In summary, our results show that visible light OCT can image age-related rod loss and remodeling at both the soma and the synapse in situ in living mice. In doing so, visible light OCT can help to provide a more complete picture of aging and retinal degeneration in the living eye.

Footnotes and Disclosures

Originally received: December 9, 2022.

Final revision: April 5, 2023.

Accepted: April 24, 2023.

Available online: April 29, 2023. Manuscript no. XOPS-D-22-00262.

¹ Department of Radiology, NYU Langone Health, New York, New York.

² Department of Biomedical Engineering, University of California Davis, Davis, California.

³ Department of Ophthalmology, NYU Langone Health, New York, New York.

Disclosure(s):

All authors have completed and submitted the ICMJE disclosures form.

The authors declare the following financial interests/personal relationships which may be considered as potential competing interests:

V.J.S.: Royalties – Optovue, Inc.

This work was supported by National Eye Institute Grants R01EY031469 (to V.J.S.), R01NS094681 (to V.J.S.), T32EY015387 (National Eye

Institute UC Davis training grant), and P30EY012576 (National Eye Institute UC Davis core grant) and Research to Prevent Blindness Unrestricted Grant (to NYU Langone Health Department of Ophthalmology).

HUMAN SUBJECTS:

No human subjects were included in this study.

Animal subjects were used in this study.

Author Contributions:

Conception and design: Kho, Srinivasan

Data collection: Chauhan, Kho, Srinivasan

Analysis and interpretation: Chauhan, Srinivasan; Obtained funding: Srinivasan

Overall responsibility: Chauhan, Srinivasan

Presented at: SPIE Photonics West Ophthalmic Technologies in 2023.

Abbreviations and Acronyms:

CNR = contrast-to-noise ratio; **ELM** = external limiting membrane; **EM** = electron microscopy; **HC** = heterochromatin clump; **LM** = light

microscopy; **NIR** = near-infrared; **ONL** = outer nuclear layer; **OPL** = outer plexiform layer.

Keywords:

Optical coherence tomography, Photoreceptors, Rods, Synapses, Aging.

Correspondence:

Vivek J. Srinivasan, PhD, Tech4Health Institute, NYU Langone Health, 433 First Avenue, New York, NY 10010 E-mail: vivek.srinivasan@nyulangone.org.

References

- Veleri S, Lazar CH, Chang B, et al. Biology and therapy of inherited retinal degenerative disease: insights from mouse models. *Dis Model Mech*. 2015;8:109–129.
- Chiu K, Chan TF, Wu A, et al. Neurodegeneration of the retina in mouse models of Alzheimer's disease: what can we learn from the retina? *Age (Dordr)*. 2012;34:633–649.
- Pennesi ME, Neuringer M, Courtney RJ. Animal models of age related macular degeneration. *Mol Aspects Med*. 2012;33:487–509.
- Gresh J, Goletz PW, Crouch RK, Rohrer B. Structure–function analysis of rods and cones in juvenile, adult, and aged C57Bl/6 and Balb/c mice. *Vis Neurosci*. 2003;20:211–220.
- Kolesnikov AV, Fan J, Crouch RK, Kefalov VJ. Age-related deterioration of rod vision in mice. *J Neurosci*. 2010;30:11222–11231.
- Cunea A, Powner MB, Jeffery G. Death by color: differential cone loss in the aging mouse retina. *Neurobiol Aging*. 2014;35:2584–2591.
- Ferdous S, Liao KL, Gefke ID, et al. Age-related retinal changes in wild-type C57BL/6J mice between 2 and 32 months. *Invest Ophthalmol Vis Sci*. 2021;62:9.
- Hermenean A, Trotta MC, Gharbia S, et al. Changes in retinal structure and ultrastructure in the aged mice correlate with differences in the expression of selected retinal miRNAs. *Front Pharmacol*. 2020;11:593514.
- Wang Y, Grenell A, Zhong F, et al. Metabolic signature of the aging eye in mice. *Neurobiol Aging*. 2018;71:223–233.
- Liets LC, Eliasieh K, van der List DA, Chalupa LM. Dendrites of rod bipolar cells sprout in normal aging retina. *Proc Natl Acad Sci U S A*. 2006;103:12156–12160.
- Samuel MA, Zhang Y, Meister M, Sanes JR. Age-related alterations in neurons of the mouse retina. *J Neurosci*. 2011;31:16033–16044.
- Cano J, Machado A, Reinoso-Suarez F. Morphological changes in the retina of ageing rats. *Arch Gerontol Geriatr*. 1986;5:41–50.
- Nadal-Nicolas FM, Vidal-Sanz M, Agudo-Bariuso M. The aging rat retina: from function to anatomy. *Neurobiol Aging*. 2018;61:146–168.
- Huber G, Beck SC, Grimm C, et al. Spectral domain optical coherence tomography in mouse models of retinal degeneration. *Invest Ophthalmol Vis Sci*. 2009;50:5888–5895.
- Ruggeri M, Wehbe H, Jiao S, et al. In vivo three-dimensional high-resolution imaging of rodent retina with spectral-domain optical coherence tomography. *Invest Ophthalmol Vis Sci*. 2007;48:1808–1814.
- Carter-Dawson LD, LaVail MM. Rods and cones in the mouse retina. I. Structural analysis using light and electron microscopy. *J Comp Neurol*. 1979;188:245–262.
- Fuchs M, Scholz M, Sendelbeck A, et al. Rod photoreceptor ribbon synapses in DBA/2J mice show progressive age-related structural changes. *PLoS One*. 2012;7:e44645.
- Li S, Mitchell J, Briggs DJ, et al. Morphological diversity of the rod spherule: a study of serially reconstructed electron micrographs. *PLoS One*. 2016;11:e0150024.
- Povazay B, Bizheva K, Unterhuber A, et al. Submicrometer axial resolution optical coherence tomography. *Opt Lett*. 2002;27:1800–1802.
- Yi J, Liu W, Chen S, et al. Visible light optical coherence tomography measures retinal oxygen metabolic response to systemic oxygenation. *Light Sci Appl*. 2015;4:e334.
- Pi S, Hormel TT, Wei X, et al. Imaging retinal structures at cellular-level resolution by visible-light optical coherence tomography. *Opt Lett*. 2020;45:2107–2110.
- Pi S, Hormel TT, Wei X, et al. Retinal capillary oximetry with visible light optical coherence tomography. *Proc Natl Acad Sci U S A*. 2020;117:11658–11666.
- Zhang X, Beckmann L, Miller DA, et al. In vivo imaging of Schlemm's canal and Limbal vascular network in mouse using visible-light OCT. *Invest Ophthalmol Vis Sci*. 2020;61:23.
- Song W, Zhang S, Kim YM, et al. Visible light optical coherence tomography of peripapillary retinal nerve fiber layer reflectivity in glaucoma. *Transl Vis Sci Technol*. 2022;11:28.
- Wang J, Nolen S, Song W, et al. Second-generation dual-channel visible light optical coherence tomography enables wide-field, full-range, and shot-noise limited retinal imaging. *bioRxiv*. 2022. <https://doi.org/10.1101/2022.10.05.511048>.
- Kho A, Srinivasan VJ. Compensating spatially dependent dispersion in visible light OCT. *Opt Lett*. 2019;44:775–778.
- Zhang T, Kho AM, Srinivasan VJ. Improving visible light OCT of the human retina with rapid spectral shaping and axial tracking. *Biomed Opt Express*. 2019;10:2918–2931.
- Kho AM, Zhang T, Zhu J, et al. Incoherent excess noise spectrally encodes broadband light sources. *Light Sci Appl*. 2020;9:172.
- Chauhan P, Kho AM, FitzGerald P, et al. Subcellular comparison of visible-light optical coherence tomography and electron microscopy in the mouse outer retina. *Invest Ophthalmol Vis Sci*. 2022;63:10.
- Srinivasan VJ, Kho AM, Chauhan P. Visible light optical coherence tomography reveals the relationship of the myoid and ellipsoid to band 2 in humans. *Transl Vis Sci Technol*. 2022;11:3.
- Curcio CA. Photoreceptor topography in ageing and age-related maculopathy. *Eye*. 2001;15:376–383.
- Jackson GR, Owsley C, Curcio CA. Photoreceptor degeneration and dysfunction in aging and age-related maculopathy. *Ageing Res Rev*. 2002;1:381–396.
- Curcio CA, Millican CL, Allen KA, Kalina RE. Aging of the human photoreceptor mosaic: evidence for selective vulnerability of rods in central retina. *Invest Ophthalmol Vis Sci*. 1993;34:3278–3296.
- Volland S, Esteve-Rudd J, Hoo J, et al. A comparison of some organizational characteristics of the mouse central retina and the human macula. *PLoS One*. 2015;10:e0125631.
- Meyer RA. Light scattering from biological cells: dependence of backscatter radiation on membrane thickness and refractive index. *Appl Opt*. 1979;18:585–588.

36. Subramanian K, Weigert M, Borsch O, et al. Rod nuclear architecture determines contrast transmission of the retina and behavioral sensitivity in mice. *Elife*. 2019;8:e49542.
37. Solovei I, Kreysing M, Lanctôt C, et al. Nuclear architecture of rod photoreceptor cells adapts to vision in mammalian evolution. *Cell*. 2009;137:356–368.
38. Zhi Z, Chao JR, Wietecha T, et al. Noninvasive imaging of retinal morphology and microvasculature in obese mice using optical coherence tomography and optical microangiography. *Invest Ophthalmol Vis Sci*. 2014;55:1024–1030.
39. Meah A, Boodram V, Bucinca-Cupallari F, Lim H. Axonal architecture of the mouse inner retina revealed by second harmonic generation. *PNAS Nexus*. 2022;1:pgac160.
40. Kar D, Kim YJ, Packer O, et al. Contributed session I: mitochondrial distribution in the outer plexiform layer of human retina - does it correlate with reflectivity in OCT? *J Vis*. 2022;22:2.
41. Fernandez-Sanchez L, de Sevilla Muller LP, Brecha NC, Cuenca N. Loss of outer retinal neurons and circuitry alterations in the DBA/2J mouse. *Invest Ophthalmol Vis Sci*. 2014;55:6059–6072.
42. Levine ES, Zam A, Zhang P, et al. Rapid light-induced activation of retinal microglia in mice lacking arrestin-1. *Vis Res*. 2014;102:71–79.
43. Kokona D, Häner NU, Ebnetter A, Zinkernagel MS. Imaging of macrophage dynamics with optical coherence tomography in anterior ischemic optic neuropathy. *Exp Eye Res*. 2017;154:159–167.
44. Fletcher EL. Contribution of microglia and monocytes to the development and progression of age related macular degeneration. *Ophthalmic Physiol Opt*. 2020;40:128–139.
45. Cuenca N, Fernandez-Sanchez L, Sauve Y, et al. Correlation between SD-OCT, immunocytochemistry and functional findings in an animal model of retinal degeneration. *Front Neuroanat*. 2014;8:151.